

Virtual Special Issue Ocean Surface Waves

On tridimensional rip current modeling



Patrick Marchesiello^{a,*}, Rachid Benshila^b, Rafael Almar^a, Yusuke Uchiyama^c,
James C. McWilliams^d, Alexander Shchepetkin^d

^aIRD/LEGOS, 14 Avenue Edouard Belin, 31400 Toulouse, France

^bCNRS/LEGOS, 14 Avenue Edouard Belin, 31400 Toulouse, France

^cKobe University, Civil Eng., Kobe 657-8501, Japan

^dUCLA, Atmos. Ocean. Sci., Los Angeles, CA 90095-1565, USA

ARTICLE INFO

Article history:

Received 13 November 2014

Revised 30 June 2015

Accepted 6 July 2015

Available online 14 July 2015

Keywords:

Rip current

Intrinsic variability

Tridimensional modeling

Video imaging

Biscarrosse beach

ABSTRACT

Do lateral shear instabilities of nearshore circulation account for a substantial part of Very Low-Frequency (VLF) variability? If yes, it would promote stirring and mixing of coastal waters and surf-shelf exchanges. Another question is whether tridimensional transient processes are important for instability generation. An innovative modeling system with tridimensional wave-current interactions was designed to investigate transient nearshore currents and interactions between nearshore and innershelf circulations. We present here some validation of rip current modeling for the Aquitanian coast of France, using in-situ and remote video sensing. We then proceed to show the benefits of 3D versus 2D (depth-mean flow) modeling of rip currents and their low-frequency variability. It appears that a large part of VLF motions is due to intrinsic variability of the tridimensional flow. 3D models may thus provide a valuable, only marginally more expensive alternative to conventional 2D approaches that miss the vertical flow structure and its nonlinear interaction with the depth-averaged flow.

© 2015 Published by Elsevier Ltd.

1. Introduction

Rip currents are narrow, seaward currents that extend from the inner surf zone out through the line of breaking waves. Rip currents are usually long (100 m), narrow (10 m) and intense jet flows (reaching 1–2 m/s). They appear to span the entire water column in the shallow breaking zone but remain confined near the surface as they flow past the breaking zone into deeper water, forming strong vertical shear (Haas and Svendsen, 2002). Understanding the complex tridimensional dynamics of rip currents remain a relevant scientific challenge as these currents play a key role on material dispersion and morphodynamics across the surfzone and are a major hazard to swimmers (see MacMahan et al., 2006, for a review).

Despite substantial evidence of tridimensional flow structure, most modeling studies of rip currents are performed using depth-integrated shallow water equations. Bruneau et al. (2011) used this class of model (MARS coupled with SWAN) to study the Aquitanian

coast of France. In June 2007 an intense 5-day field experiment was conducted at the mesotidal/macrotidal wave-dominated Biscarrosse Beach on a well-developed bar and rip morphology. Previous analysis of the field data exposed the main characteristics of a tide-modulated rip current driven by low- to high-energy shore-normal waves (Bruneau et al., 2009b). The model was able to reproduce some of the rip current characteristics but discrepancies with observations were evidenced at the rip neck, this narrow jet-like region where the rip current velocity is maximum.

In a parallel study, Bruneau et al. (2009a) showed occurrence of rip current variability, referred to as Very Low Frequency motions (VLF), in the rip neck where VLF pulsations were most intense (reaching 1 m/s on time scales of 10–30 min). These oscillations were consistent with shear instabilities similar to those produced by the analytical solution of Haller and Dalrymple (2001). Intrinsic variability of the nearshore circulation is an alternative to vorticity generation by short-crested wave breaking (Peregrine, 1998; Spydell and Feddersen, 2009) or low-frequency wave forcing (Long and Özkan-Haller, 2009), but the contribution of each component is highly debated.

In this paper, we extend on the work of Bruneau et al. (2011); 2009a) to show that tridimensional dynamics must be accounted

* Corresponding author. Tel.: +33 5 61 33 29 38.

E-mail address: Patrick.Marchesiello@ird.fr, Patrick.Marchesiello@legos.obs-mi.fr (P. Marchesiello).

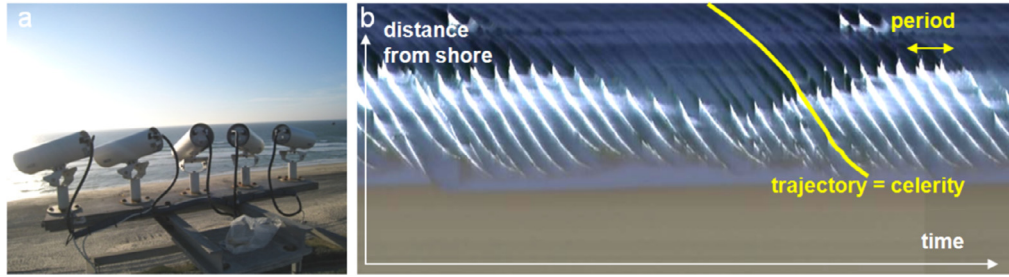


Fig. 1. Coastal video monitoring: description of applications; (a) 5-camera system for Biscarrosse (France); (b) Spatial-temporal post-processed image showing wave dynamics. The image is generated from the high frequency acquisition of a cross-shore array of pixels.

for in the study of rip currents, i.e., in their persistent structure and instability behavior. Our results are relevant to the ongoing discussion on intrinsic and extrinsic origins of VLF energy. Before addressing these points, we present our model setup and calibration technique, relying on breaking wave dissipation patterns provided by video monitoring.

2. Methods

2.1. Video monitoring

A main limitation for understanding nearshore processes is lack of appropriate observation. Traditional *in situ* measurement techniques can provide high sampling rates and a direct estimation of many parameters, but with coarse spatial resolution that often misses complex dynamical interactions. In addition, instruments must be deployed in high-energy and sometimes hazardous environments (wave-breaking, strong currents), endangering not only the instruments, but also the personnel involved. As an alternative, remote sensing techniques can provide synoptic coverage over large areas with a wide range of temporal and spatial resolutions.

The video imaging technique (Holman and Haller, 2013) is particularly suited to coastal observation thanks to low-cost and easy deployment and maintenance of the camera-based technology. It is also considered as a non-disruptive observation technique for nearshore research. A video system was deployed at Biscarrosse beach in 2007 (Almar et al., 2009; Fig. 1) and inversion methods were revisited to provide estimation of the complete nearshore system, i.e., hydrodynamics (wave characteristics, water level, currents and breaking wave dissipation rates) and morphodynamics (shoreline, sub- and intertidal bathymetry) continuously and over long-term periods and large areas (approximate 2×1 km). Here we only use information on wave breaking dissipation.

Time-exposure images were generated by averaging over 1200 consecutive images (10 min) four times per hour during daylight. The 5-camera images were rectified from pixel to world coordinates (Holland et al., 1997) and merged to yield a single plan view image referenced to the tidal level. The grid resolution in the plan view images is 2 m (over the inner-bar area facing the video cameras, the pixel footprint is about 0.5 and 1 m in alongshore and cross-shore directions, respectively; it increases to about 10 and 20 m at both alongshore ends of the field site). When time-exposure images are of good quality (e.g., no sunglint), wave-breaking over the underlying sand bar morphology is revealed by a smooth band of white. After removing the background pixel intensity value, the normalized light intensity field can be used as a proxy of wave energy dissipation rate (Almar et al., 2010; Haller and Catalán, 2009; Lippmann and Holman, 1989).

2.2. The model

The objective of the paper is to assess the benefit of tridimensional coastal models. An innovative modeling approach for 3D wave-

current interactions (McWilliams et al., 2004) was implemented in the Regional Oceanic Modeling System (ROMS; Shchepetkin and McWilliams, 2005) by Uchiyama et al. (2010) and used for an idealized study of longshore current shear instability (Uchiyama et al., 2009). An upgraded implementation is proposed here for the AGRIF version of ROMS (Debreu et al., 2012; Penven et al., 2006). It allows additional capabilities such as nesting and wetting/drying (Warner et al., 2013), the latter being crucial to the meso- macro-tidal environment of Biscarrosse beach.

ROMS is a hydrostatic, incompressible, free-surface and terrain-following coordinate model with non-conservative forcing, diffusion, and bottom drag. It uses baroclinic/barotropic mode splitting, with explicit fast time-stepping and subsequent conservative averaging of barotropic variables. The discretization is with high-order finite differences that provide both accurate and cost-effective solutions.

The interaction of surface gravity waves and currents is implemented in ROMS through vortex-force (VF) formalism. Eulerian wave-averaged current equations for mass, momentum, and tracers are included based on an asymptotic theory by McWilliams et al. (2004) plus non-conservative wave effects.

The advantage of the vortex-force over radiation-stress formalism is to cleanly separate conservative and non-conservative effects on currents; it also unfolds the vortex force and Bernoulli head components of conservative effects. Material advection by Stokes drift is another important conservative effect. The non-conservative components (acceleration / dissipation) are those that require parameterization and are thus responsible for the largest uncertainties in our model formulation. Clear identification of these terms is thus of primary interest. Another advantage of the VF formalism is numerical since it requires taking one fewer derivative in space and thus produces fewer numerical approximations (Weir et al., 2011).

Non-conservative wave effects are due to wave breaking, associated surface roller waves, bottom streaming, and wave-enhanced vertical mixing and bottom drag. The nonlinear parameterization of Soulsby (1995) for wave-enhanced bottom drag is particularly relevant to the present case with strong tidal flow:

$$\bar{\tau}_b = \bar{\tau}_c \left[1.0 + 1.2 \left(\frac{|\bar{\tau}_w|}{|\bar{\tau}_w| + |\bar{\tau}_c|} \right)^{3.2} \right] \quad (1)$$

with

$$\bar{\tau}_c = \rho_0 \frac{\kappa^2}{\left[\ln \left(\frac{z_r}{z_0} \right) \right]^2} |\bar{\mathbf{u}}| \bar{\mathbf{u}} = \rho_0 C_D |\bar{\mathbf{u}}| \bar{\mathbf{u}} \quad (2)$$

and

$$|\bar{\tau}_w| = \frac{1}{2} \rho_0 f_w |\bar{\mathbf{u}}_w|^2 \quad (3)$$

$\bar{\tau}_c$ and $\bar{\tau}_w$ are bottom stresses due to currents and waves; κ is Von Karman constant; z_r is the bottom-most grid cell height (for horizontal velocities); z_0 is bottom roughness (taken here as 1 cm); f_w is a wave

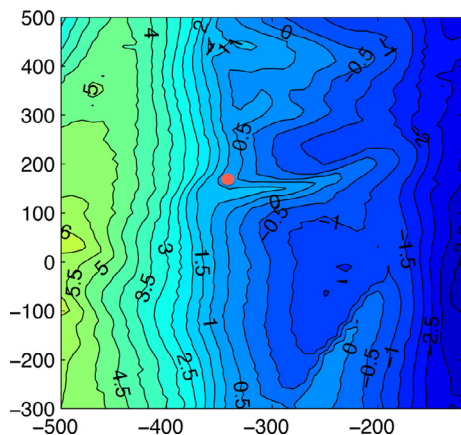


Fig. 2. Model domain and interpolated bathymetry. The orange dot shows the measurement station S4 at the rip neck where model-data comparisons are presented. The cross-shore and alongshore distances are relative to the video camera position on the beach. The 0 isobath indicates the lowest astronomical tide.

friction factor dependent on bottom wave orbital velocity $|\bar{u}_w|$ and wave frequency (see [Blaas et al. \(2007\)](#), for details on ROMS implementation). All other parameterizations are described in [Uchiyama et al. \(2010\)](#).

The currents are coupled with a ray-theory spectrum-peak wave propagation model (WKB model) describing wave crest conservation with wave refraction and conservation of both wave and roller action (wave rollers cause a lag in the transfer of momentum to the currents in the wave breaking process). The wave model includes the Doppler-shifted current effect on waves and dissipation due to shoaling-induced wave breaking and bottom drag. A description is given in [Uchiyama et al. \(2010\)](#) and [Weir et al. \(2011\)](#), who used it for an idealized study of rip currents using the vortex-force formalism. The system is thus fully coupled within a unique executable code that is both convenient and computationally efficient.

2.3. Biscarrosse beach setup

Biscarrosse Beach is located along the Aquitanian coast of southwest France, exposed to the powerful North Atlantic swell. The wave climate is characterized by a mean offshore significant wave height of 1.4 m, mean period of 6.5 s and mean West-North-West direction ([Butel et al., 2002](#)). The tide is semi-diurnal, with neap and spring tidal ranges of 2 and 5 m, respectively (i.e., meso-macro tidal range). Biscarrosse Beach is mostly intermediate double-barred following the classification of [Wright and Short \(1984\)](#). The inner bar in the intertidal zone exhibits a transverse bar and rip morphology with mean rip spacing of about 400 m ([Castelle et al., 2007](#)).

The coupled model is applied to the nearshore zone of Biscarrosse Beach during the 2007 field measurement campaign (see bathymetry in [Fig. 2](#)). From an ADCP deployed in 10 m water depth (at low tide), offshore measurements of tidal elevation, wave height and winds¹ are used to force the model for 5 days from the 13th to the 17th of June 2007. The tidal range varied from 3.3 to 3.8 m, the offshore significant wave height from 0.5 to 3 m (mostly swell), peak wave period from 8 to 11 s, and wave angle often close to shore normal ([Bruneau et al., 2011; 2009b](#)). Open boundary conditions must handle outgoing perturbations generated inside the computational domain while external forcing is specified. To that end, we use a combination of characteristic methods for barotropic tides and radiation equations for baroclinic currents, with the addition of Newtonian and viscous

damping ([Marchesiello et al., 2001](#)). Offshore waves are simply specified, as coastal reflection is negligible.

The horizontal resolution is 5 m for the standard simulation but sensitivity tests are usually done at a lower resolution of 10 m. In addition, a simulation at 20 m resolution allows us to test the convergence of numerical solution. On the vertical, there are 20 terrain-following (sigma) levels equally spaced and the water has a constant density ρ_0 (there is no surface or lateral buoyancy forcing). The horizontal eddy viscosity is given by the flow- and resolution-dependent [Smagorinsky \(1963\)](#) formulation:

$$\nu_T = (C_S \Delta)^2 |S|, \quad (4)$$

where S is the strain rate, Δ the model horizontal resolution and C_S the Smagorinsky coefficient. With a standard value of $C_S=0.1$, ν_T is always lower than $1 \text{ m}^2/\text{s}$ in our simulations (this point is discussed in [Section 5](#)). The baroclinic time step is 2 s and 30 barotropic sub-steps are performed every baroclinic step. The cost of 3D computations is thus moderate and the full 3D model is only marginally more expensive than the 2D part².

3. Calibration and validation

In the following, the model is calibrated using video data and the results are compared with *in situ* observations for validation.

3.1. Calibration with video data

There is still no consensus on many parameterizations: breaker acceleration and turbulent mixing, contribution of the breaking wave roller, bottom friction and boundary layer streaming (e.g., [Uchiyama et al., 2010](#)). In particular, the parameterization of breaking wave dissipation is crucial to nearshore dynamics but is generally guided by scarce data. One novelty of our method lies in the tuning of breaking wave dissipation in the wave model by direct comparison with video images.

The wave model uses the parameterization of [Church and Thornton \(1993\)](#), which has the particularity of producing more shoaling of the incoming wave before breaking and thus more intense breaking than other available choices ([Weir et al., 2011](#)):

$$\epsilon_b = \frac{3\sqrt{\pi}}{16} \rho_0 g f_p B_b^3 \frac{H_{rms}^3}{D} \left[1 + \tanh \left\{ 8 \left(\frac{H_{rms}}{\gamma_b D} - 1 \right) \right\} \right] \times \left[1 - \left\{ 1 + \left(\frac{H_{rms}}{\gamma_b D} \right)^{-\frac{5}{2}} \right\} \right] \quad (5)$$

f_p is the peak frequency of the waves, H_{rms} is the root-mean-square wave height (twice the amplitude), and D the bottom depth. This parametrization relies on two empirical constants: the breaking wave parameter γ_b is the wave height-to-depth ratio for which all waves are assumed to be breaking and B_b is the fraction of foam on the face, accounting for the type of breaker.

10 min average video recording provides a high-resolution and statistically reliable image of the wave breaking pattern. [Fig. 3](#) (top panels) shows two examples for low- and high-energy conditions on June 14 and 16 respectively. Under the assumption that light intensity varies as the dissipation of the incident wave, the video patterns can be compared (after normalization by rescaling between 0 and 1) with the model patterns of wave dissipation ([Fig. 3](#), bottom panels). We tested various combinations of the two breaking parameters γ_b and B_b and visually estimated a best fit to cross-shore patterns

¹ The wind effect on nearshore circulation is weak overall during the experiment and will not be discussed further here.

² We use 144 CPUs (on an IBM Power computer at the French IDRIS center) to integrate the 5 m resolution model on $187 \times 205 \times 20$ grid points. The elapsed time for the 5 day simulation is about 7 h. It is 6 h with the equivalent 2D model (only the depth-averaged part of the equations is integrated in this case). We thus estimate the cost of the 3D model as only 15% higher than the 2D model.

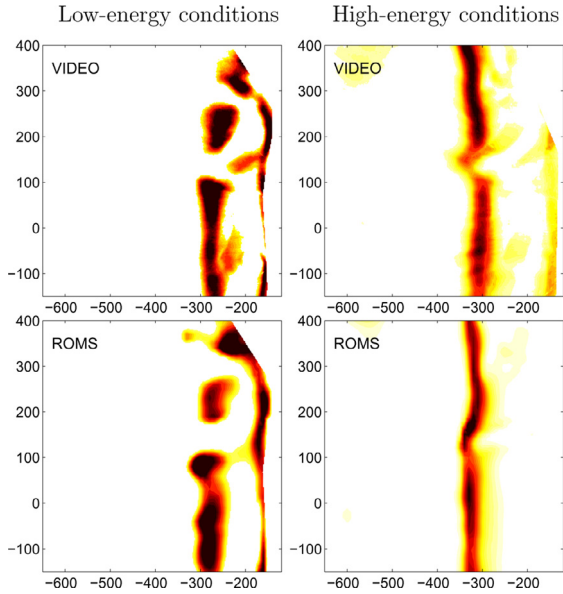


Fig. 3. Normalized wave-breaking dissipation from 10 min averaged video data (top panels) and ROMS (bottom panels) after calibration (color range is from 0 to 1 with dark shades indicating higher values). Two examples are given: one for low-energy conditions (June 14 at 8:45 LT; left panels) and the other for high energy conditions (June 16 at 12.00 LT). On the first example, classical features of dissipation appear: high dissipation rates over the intertidal sand bar and near the shoreline with minimum dissipation in the trough and rip channels. At high-energy conditions, breaking occurs further offshore with less alongshore variability; some breaking also occurs over the subtidal bar around 600 m from shore (yellow patches in the upper left corner). (For interpretation of the references to color in this figure legend, the reader is referred to the web version of this article).

– looking especially at surfzone width and position – given by the clearest video images. This method is suboptimal compared with data assimilation techniques (currently under development) but proved successful. Values of 0.3 and 1.3, for γ_b and B_b respectively, provide the best fit from our experience. There is no need here to add a time dependence on γ_b as the fit to data appears valid for both low- and high-energy conditions (Fig. 3), justifying the use of Eq. 5 from Church and Thornton, 1993. The fraction α_r of breaking waves converted into rollers is taken as 0.5 and reveals only little sensitivity.

3.2. Validation with in-situ data

Fig. 4 presents a model-data comparison for wave height and cross-shore currents at station S4 located on the edge of the rip neck (see Fig. 2; the S4 Interocean electromagnetic current meter acquired velocity data about 40 cm above ground at a 2 Hz sample rate). The observation shows a strong increase of wave height on the 15th of June due to offshore forcing but strongly modulated by large tides (with range of close to 4 m) that shift back and forth the cross-shore position of the breaking line. High-energy conditions from June 15th lead to strong offshore-directed rip currents in excess of 75 cm/s.

The model is able to reproduce the wave height evolution (Fig. 4, upper panel; Corr=0.95; RMSE=13 cm). The fit is quite remarkable during high-energy conditions. The directional wave spectra presented in Bruneau et al. (2009b) is composed of narrow-banded swell during both low- and high-energy conditions (in the latter case, superimposed on a large directional spread of weaker wind waves). Therefore, the assumption is validated that nearshore waves in this experiment are well described by ray equations driving a single wave with root-mean-square wave height and frequency corresponding to the spectral peak.

There is an equally remarkable fit of simulated currents with data (Fig. 4, lower panel; Corr=0.83; RMSE=14 cm/s). A series of rip events are present in both model and observations and are correlated with

tides. Here, rip events appear as burst of momentum during flood and ebb phases (maximum currents are reached between low- and mid-tide of each phase) separated by periods of inactivity at high tides. Therefore, rip currents have a dual cycle of tidal and semi-tidal periods. During events, shifting negative and positive velocities are observed at S4 because it is on the northern edge of the rip channel in a transitional position between shoreward and seaward flow (setting up a mooring in the channel is a real challenge). If rip events appear as tidally-driven slow variations of cross-shore currents, faster oscillations are present as well, most prominent during rip events; they will be treated in Section 5.

Because of strong horizontal and vertical shear at S4, the model-data comparison is sensitive to both vertical and horizontal interpolation of the model solution to the measurement point. The sensor's vertical displacement must be accounted for (its position varies in time between 30–40 cm above the sea floor). This being considered, the match is excellent in terms of correlation and standard deviation, in contrast with known 2D simulations (Bruneau et al., 2011, their Fig. 7).

4. Rip current sensitivity to the vertical dimension

4.1. Comparison with a two-dimensional simulation

To analyze the extent of errors related to the shallow water hypothesis, we now compare our standard solution with a two-dimensional version of ROMS. In this case the barotropic mode is advanced alone. Note that the cross-shore barotropic flow (depth-averaged \bar{u}) of the 2D model is different from that of the 3D model because the latter receives contribution from the baroclinic flow u' :

$$\frac{\partial \bar{u}}{\partial t} = - \left[\frac{\partial \bar{u}\bar{u}}{\partial x} + \frac{\partial \bar{u}\bar{v}}{\partial y} \right] + \overline{VF} + f\bar{v} - g \frac{\partial \eta}{\partial x} + F_u + D_u - \frac{\tau_b}{\rho_0 H} - \left[\frac{\partial \overline{u'u'}}{\partial x} + \frac{\partial \overline{u'v'}}{\partial y} \right] - \frac{1}{\rho_0} \frac{\partial \bar{P}}{\partial x} \quad (6)$$

The first line of Eq. 6 contains the terms of a wave-averaged shallow water model: time rate, advection, vortex force, Coriolis force, pressure gradient (inclusive of wave effects on surface pressure, e.g. setup/setdown), external forcing (wind stress, wave-breaking and bottom streaming), lateral dissipation and bottom friction. The second line contains the coupling terms between barotropic and baroclinic modes, i.e., the baroclinic contribution to nonlinear advection (divergence of baroclinic Reynolds stresses of type $\overline{u'u'} = \bar{u}\bar{u}' - \bar{u}\bar{u}$) and the depth-averaged internal pressure gradient. We neglect the latter here as we assume no stratification but it may be of importance out of the surf zone (Hally-Rosendahl et al., 2014).

For the bottom drag due to currents³, we can derive an equivalent formulation to the 3D case, assuming that in shallow water the logarithmic layer extends all the way to the surface. In this case, integrating the velocity profile provides a 2D drag coefficient of the form:

$$C_D = \left(\frac{u^*}{|\bar{u}|} \right)^2 = \left(\frac{u^*}{\frac{1}{H} \int_0^H \frac{u^*}{\kappa} \ln \frac{z}{z_0} dz} \right)^2 = \frac{\kappa^2}{\left[\ln \frac{H}{z_0} - 1 \right]^2} \quad (7)$$

where H is total depth and u^* the friction velocity. Eq. 7 would ensure that the 2D bottom stress equals that of the 3D model for the same barotropic flow. This, however, turns out to be wrong: the 2D drag coefficient in Eq. 7 is too weak for 2D and 3D bottom drags to match. A closer match (also between the 2D model circulation and observations) is obtained with a constant linear coefficient of 0.0025 m/s in the 2D model. This is a first indication that the nearshore circulation

³ The bottom stress due to waves has no dependence on the vertical grid and is the same in 2D and 3D models.

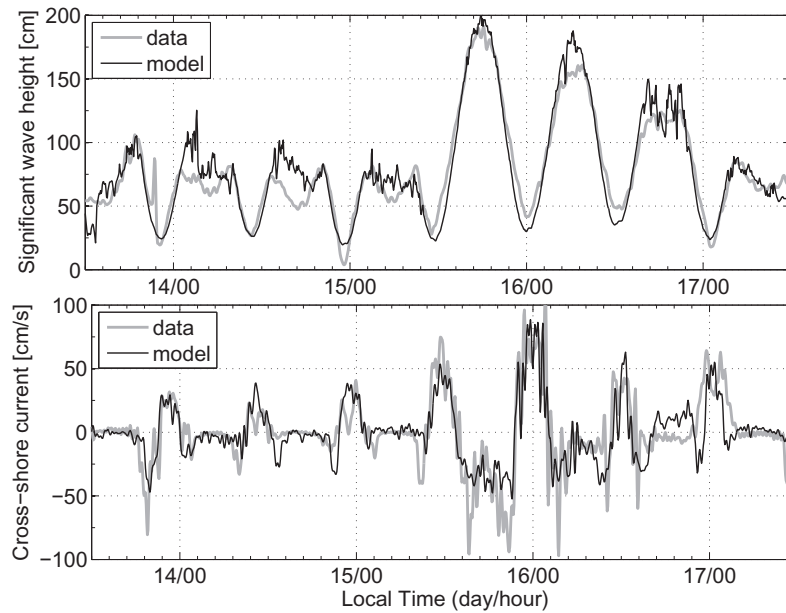


Fig. 4. Model-data comparison at station S4 for significant wave height (top) and cross-shore currents (bottom) for the period of June 2007 campaign (the sign convention is positive for shoreward currents.). A low-pass filter with a cutoff period of 30 min is applied to the observed and modeled currents.

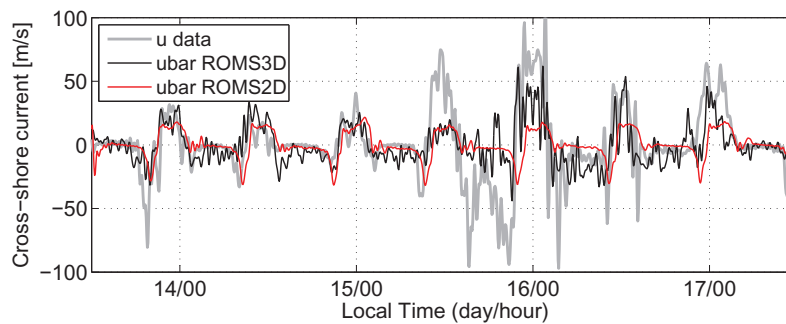


Fig. 5. Depth-averaged component of cross-shore velocity in ROMS2D and ROMS3D compared with total velocity from observational data (see Fig. 4 for total velocity from the model).

off Biscarosse Beach is poorly approximated by a 2D flow with logarithmic layer, as confirmed below.

Fig. 5 shows a comparison of the barotropic components of ROMS in its shallow water and 3D versions. It appears that the shallow water model yields weaker correlations with data and clearly underestimates the cross-shore flow, especially during high-energy conditions (RMSE between observations and model estimates is then larger by a factor of 2.5). Over the whole time series, the standard deviation of \bar{u} at S4 is about 10 cm/s in the 2D model compared with 22 cm/s for u in the 3D model and 26 cm/s in the observations. Interestingly, the barotropic mode of the 3D model shows larger velocities (14 cm/s standard deviation), especially during high-energy conditions, implying a significant role played by the baroclinic contribution to barotropic nonlinear terms.

4.2. Analysis of 2D/3D coupling

To analyze the 2D/3D coupling effect, we choose a low-energy rip event (June 14 around 9 a.m.) that is isolated from surrounding flow systems (in contrast, high-energy conditions show frequent interactions). Fig. 6 presents instantaneous maps of baroclinic Reynolds stress $\overline{u'u'}$ and associated divergence term $-\partial\overline{u'u'}/\partial x$ (the other term is weaker). The Reynolds stress field is a measure of vertical shear variance showing that departure from depth-averaged flow is significant everywhere in the surf zone and along the rip current. The

Reynolds stress divergence is the baroclinic part of advection that exchange momentum between the baroclinic and barotropic circulation. In Fig. 6, the rip neck stands as a location of positive advection, i.e., the surface current and vertical shear are accelerated along the seaward rip current at the expense of the depth-averaged flow (increase of \bar{u} but weakening of $|\bar{u}|$ since $\bar{u} < 0$).

Fig. 7 compares baroclinic advection to the other terms of the depth-averaged cross-shore momentum budget (Eq. 6). As a whole, rip current system dynamics (right panel of Fig. 7) result from a balance between breaker acceleration, advection and pressure gradients (vortex force, bottom drag and streaming are not negligible but lesser players). Wave breaking accelerates the seaward flow over sand bars and builds a strong pressure gradient that pushes the rip current in the feeder zone.

The rip current is then advected from the feeder zone (250–300 m) to the rip neck (300–350 m) as confirmed by looking more specifically at the momentum budget along the rip channel (bottom panel of Fig. 7): barotropic advection goes from positive (rip deceleration) to negative values (acceleration). In the feeder zone, the current is barotropic as illustrated by a section of cross-shore currents (Fig. 8; left panel) but as water deepens further offshore, baroclinic advection becomes a major player. Its strong positive values in the rip neck indicate a conversion from barotropic to baroclinic currents. About half of the barotropic flow advected to the neck area is converted into baroclinic flow. This is associated with a strong increase of

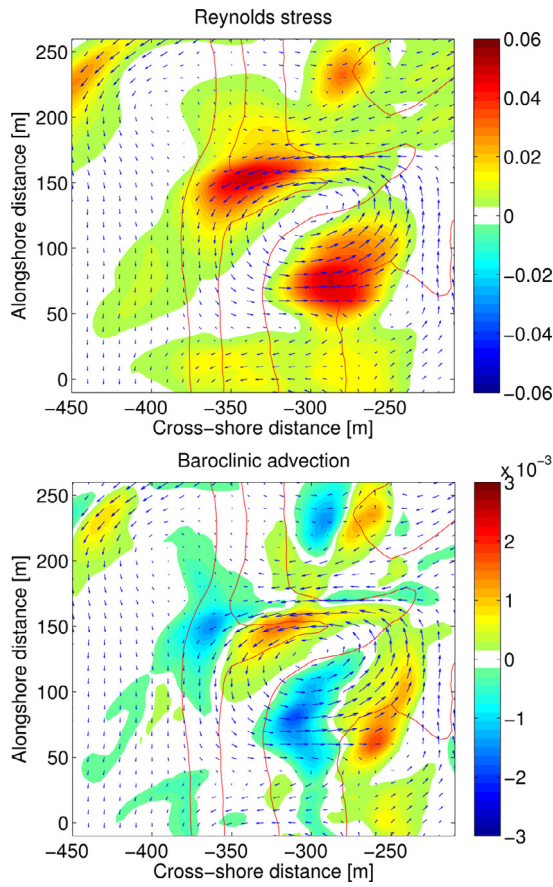


Fig. 6. Baroclinic Reynolds stress $\overline{u'u'}$ in m^2/s^2 (top) and its divergence, i.e. baroclinic advection, in m/s^2 (bottom) during the low-energy period. Depth-mean velocity vectors are overlaid.

vertical shear (Fig. 8), reminiscent of laboratory measurements by Haas and Svendsen (2002, e.g., their Fig. 12). As a result, the surface flow keeps its speed along the channel while the barotropic flow is largely reduced, a process called surface confinement or trapping (Shepard et al., 1941). During this process, bottom currents and drag are considerably reduced and even reversed (Fig. 7 and 8).

Interestingly, the barotropic current is also decelerated in the neck area by a positive pressure gradient. The latter results from wave shoaling enhanced by the surface rip current, which has thus

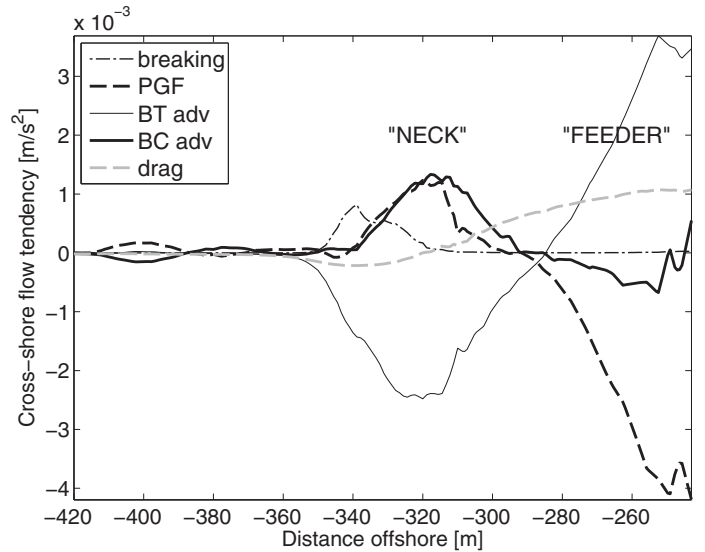
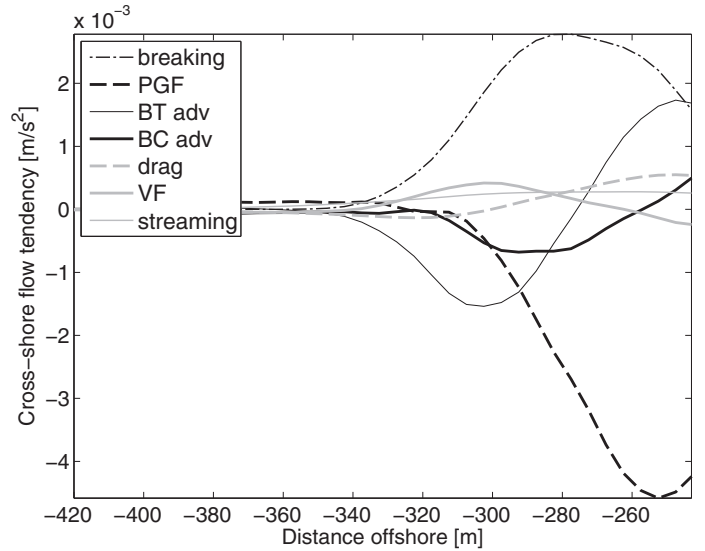


Fig. 7. Depth-averaged cross-shore momentum budget for the low-energy period of the entire rip system (top; averaged over a 300 m longshore distance around the rip channel) and along the rip current (bottom). Note that positive values of budget terms indicate a tendency to accelerate shoreward currents and decelerate seaward (rip) currents. The advection term is split between its barotropic (BT) and baroclinic (BC) parts. BC advection is shown by a thick black line.

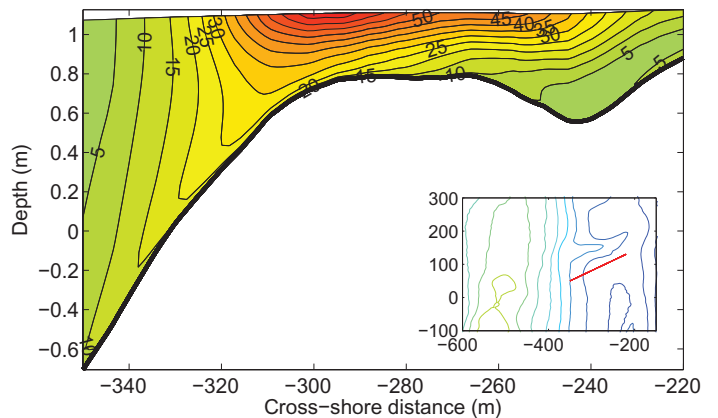
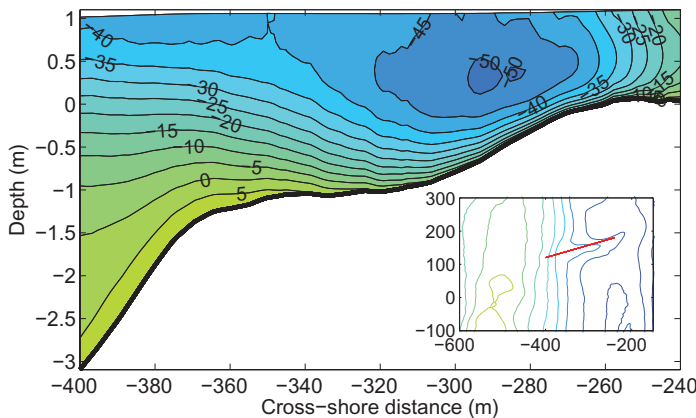


Fig. 8. Snapshot (June 14 at 9 a.m.) of cross-shore currents along the rip channel (left) and sand bar (right); section locations are drawn in the inset. Note the strong shear generated seaward along the rip current, with current reversal near the bottom as in the laboratory measurements of Haas and Svendsen (2002). The right panel shows the profile of breaking-wave-driven onshore flow.

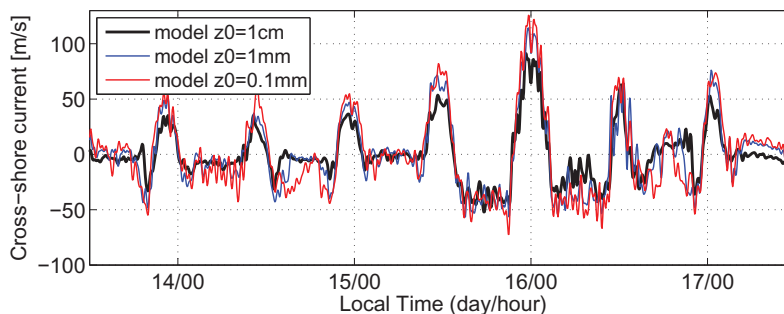


Fig. 9. Model sensitivity to bottom roughness length z_0 at station S4. The model resolution is 10 m here and z_0 varies from 1 cm (standard case) to 1 mm and 0.1 mm. The standard case is the same as in Fig. 4 and is the closest to observations).

a negative feedback effect on depth-averaged rip currents (Weir et al., 2011; Yu and Slinn, 2003).

Large Reynolds stress values are also evidenced over sand bars in the onshore flow region of the rip system (Fig. 6). They are related to the circulation formed by a strong surface onshore flow and opposing seaward acceleration by pressure gradients (Fig. 8; right panel). Baroclinic advection seems to act in this case as a redistribution process that increases barotropic flow in the inner surf and feeder zones, at the expense of the outer surf zone. The increased barotropic flow is then advected to the rip neck by the depth-averaged recirculation. Therefore, the larger rip neck transport in the 3D versus 2D simulation (Fig. 5) is not locally generated but provided by the strong recirculation system, which redistributes surface-trapped currents into the rip feeder zone.

These results are relevant to modeling strategies, as they imply that nearshore circulation cannot simply be addressed by linear combination of a depth-averaged model and a vertical profile technique, a common approach in morphological models (e.g., De Vriend and Stive, 1987).

4.3. Sensitivity of the 3D solution

The vertical structure of the 3D flow has several dependencies. In particular, it is affected by the profile distribution function of breaking and roller acceleration. As for Uchiyama et al. (2010), the best fit to data is obtained with a surface-intensified breaking force (varying as $\cosh[(z+D)/(a_b H_{rms})]$, where a_b is a constant set to 0.2), that allows an undertow to develop over the bar crests.

The model results are also sensitive to the bottom roughness length z_0 used in the parametrization of bottom stress due to currents (Eq. 2). Its impact on the magnitude of cross-shore currents is shown in Fig. 9. A relatively large roughness value of 1 cm (our reference value) provides a good match with data, while lower values tend to produce excessive flow speed. Roughness lengths of 1 mm and 0.1 mm produce standard deviations of 32 and 36 cm/s respectively, i.e., higher than the 26 cm/s value observed. In contrast, the current's magnitude is weakly affected by lateral viscosity (not shown) unless very high values of the Smagorinsky coefficient ($C_S=1$) are used. These conclusions hold for the steady part of rip currents (i.e., slowly varying with tide and wave forcing) and higher frequencies are explored in the following.

5. Rip current instabilities

Very Low Frequency (VLF) motions are described as ubiquitous slow oscillations of the nearshore circulation at periods longer than 5 min (and with uncertain upper limits), i.e., slower than infragravity waves referred to as low-frequency motions (MacMahan et al., 2004). Shear instability of longshore currents are generally admitted as an important process for VLF generations, but for rip currents an important part of the literature associates VLF motions with modula-

tion of the wave forcing (Long and Özkan-Haller, 2009; Spydell and Feddersen, 2009). Yet, Kennedy (2003) suggests that wave group-forced rip current pulsations may be more active on timescales of several minutes than 10 s of minutes. Intrinsic instabilities of rip currents are thus potentially important for slow pulsations. Our single-wave forcing approach (wave forcing varies at time-scales longer than 2 h in the model) is suited to explore that part of VLF motions and quantify it by comparison with data.

5.1. Background

Haller and Dalrymple (2001) developed an analytic depth-averaged model to study the linear spatial stability of a rip current⁴ and show that low-frequency oscillations can be explained by shear-flow (vortical) instabilities. In absence of friction and bottom slope, the results are consistent with those of the classical Bickley jet⁵ (Bickley, 1939). The fastest growing sinuous mode of Haller and Dalrymple (2001) produces jet meandering with non-dimensional wavenumber $k^*=0.639$ and frequency $\sigma^*=0.255$, related to actual wavenumber k_0 and frequency σ_0 by length and vorticity scales, i.e., oscillation wavelength and period given by:

$$L_0 = \frac{2\pi}{k_0} = \frac{2\pi l}{k_*}, \quad T_0 = \frac{2\pi}{\sigma_0} = \frac{2\pi l}{\sigma_* U_{max}}, \quad (8)$$

Here, U_{max} is the maximum jet velocity and l its half-width length-scale. The oscillation frequency of a rip current is thus closely controlled by the magnitude of its vorticity, a result supported by laboratory experiments (Kennedy and Zhang, 2008). With rip currents of 0.2–0.7 m/s and jet half-width of 20 m, the time-scale can span a range of 10–40 min (and wavelength of about 200 m), with faster oscillations for stronger rips. In Haller and Dalrymple (2001), viscosity, bottom friction and bottom slope play a large role in controlling vorticity (through offshore jet spreading) and thus the instability process. In general, friction has a strong stabilizing effect and would increase the period of unstable oscillations. The bottom slope has a similar effect. Although vortex stretching tends to reduce jet spreading (as opposed to bottom friction), continuity of the depth-averaged flow has a stronger effect in reducing jet speed. In the tridimensional problem, surface trapping past the surf zone would be less sensitive to both vortex stretching and continuity effects but with uncertain outcome on the overall contribution of bottom slope to jet vorticity.

If the angle of incidence of the waves is nearly shore-normal (below about 3°), a negative feedback of rip currents on wave forcing is known to reduce their cross-shore extension and concentrate their

⁴ Exponential growth of normal modes along the jet axis is considered with real frequency and complex wave number.

⁵ The Bickley jet is a parallel flow with profile function $\text{sech}^2 = 1/\cosh^2$ about the centerline and has inflection points (change of sign of vorticity gradients) satisfying the Rayleigh criterion for shear-flow instability. It produces two types of unstable modes: sinuous and varicose.

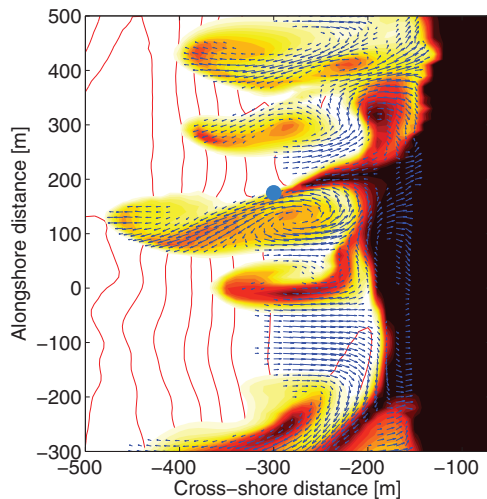


Fig. 10. Snapshot (June 14 around 10 a.m.) of surface flow (vectors) carrying a passive tracer initially released in 1 m depth (black shade). Station S4 is marked by a blue spot at the neck of a rip current. A mushroom-shaped pattern at the rip head. Plot axes are cross-shore and longshore distances. (For interpretation of the references to color in this figure legend, the reader is referred to the web version of this article).

energy nearshore (Özkan-Haller and Li, 2003; Weir et al., 2011; Yu and Slinn, 2003). Kennedy and Zhang (2008) developed a stability analysis including such wave-current interactions. The rip feedback on wave forcing is shown to reduce the offshore extension of both sinuous and varicose modes. Some of these sinuous modes may explain the fluctuating circulation cell described by MacMahan et al. (2004). In addition, Kennedy and Zhang (2008) expose a slower pulsation due to a wave-current-type instability that develops for small wave heights (also seen in the numerical experiments of Haas et al., 2003). Wave-current modes are a transient (non-equilibrated) expression of the negative feedback mechanism between rip current and wave breaking⁶. These modes have periods longer than shear instabilities (beyond 30 min) and may develop downstream of the jet, much as a convective instability. However, their role in realistic configurations is uncertain.

5.2. Modeled instability event off Biscarrosse

Fig. 10 shows a snapshot of rip current flow advecting a passive tracer. The general pattern shows a rip flow biased towards the south and a strong cyclonic recirculation cell, very similar to that of Haas et al. (2003). It also suggests the presence of turbulence, i.e., meandering and offshore-developing instability with a mushroom-shaped pattern detaching from the rip recirculation cell. Fig. 11 shows the instability development with a filament of negative vorticity meandering as it propagates offshore, much like the sinuous mode of Haller and Dalrymple (2001). Maximum vorticity within the rip current is larger than 0.05 s^{-1} , which is on the order of the vorticity scaling used in the previous section. A time- and length-scale estimation of this instability event is around 30 min and 200 m respectively, consistent with Eq. 8. It is an illustration of VLF modes produced in the model.

5.3. Observation spectrum

Bruneau et al. (2009a) noted VLF oscillations in Biscarrosse time-series with periods of 10–30 min. Low-pass filtering of the data (at

S4 in the rip neck) indicates that these VLF oscillations are correlated with the presence of rip currents (Fig. 12). This is also true for the model but, while its skills are excellent at predicting the phase of slow variations associated with rip events (given tide and wave forcing), single VLF oscillations in the model are not coincidental with observed events.

For further comparison with the model, it may be useful to analyze the rip current frequency spectrum. However, the power spectrum in Fig. 13 is broad and shows energy at all frequencies, increasing for slower oscillations; peak frequencies are blurred by abrupt transitions projecting over the whole spectrum. These are due to the location of S4 station on the edge of the rip channel, which sees fast flow reversal as the rip current shifts position during tidal ebb and flood cycles.

A Morlet wavelet analysis is presented in Fig. 14 that shows the distribution of signal energy during the first three rip events. Again, the patterns tend to reflect sharp transitions during rip events projecting over a wide range of scales. Yet, physically meaningful oscillations are apparent at the tidal and half-tidal frequencies, as they affect breaking conditions around the rip channel (given by $\gamma_b > 0.3$ and represented in red color in the time-series of Fig. 14). More importantly here, energy peaks are present in the VLF range and are only apparent during rip events (consistent with Fig. 12).

5.4. Model spectrum

In the model, the Fourier and wavelet transforms are in agreement with observations although the amplitude is lower, especially in the VLF range (Fig. 12). Yet, the model reproduces a large part of the observed VLF signal. Since VLF motions are intrinsic in the model, our results suggest that substantial VLF energy is provided in the real coastal ocean by intrinsic rather than extrinsic processes.

Similarly to observations, peak VLF amplitudes in the model are correlated with rip current events (Fig. 14, left panels). There is an apparent model-data mismatch of the relative peak VLF amplitudes in different events (bottom panels of Fig. 14; e.g., larger amplitude is seen during the first observed event in the data, during the second in the model). Part of the discrepancy may be due to model error in reproducing mean rip events and thus mean-eddy conversion. Another part is stochastic since VLF motions arising from instability processes feed from rip currents but with unpredictable outcome. Specifically, there are less than 8 VLF oscillations during each rip event, which produces for a particular rip event more than 50% error on VLF variance (assuming normal distribution)⁷.

We note that in contrast to observations, the model produces a background of VLF energy that is apparent at high tides between rip events (see in particular the black part of time-series curve in Fig. 14). This phenomenon seems associated with long meandering jets emerging from the shore break at high tides (clearly visible on animations of surface currents). Because it is absent from the data, we conclude that this high-tide VLF signal is spurious and presumably results from insufficient model dissipation in the swash-zone. A parametrization of swash zone dynamics (Antuono et al., 2007; Brocchini and Bellotti, 2002) will be part of future model developments.

Next, to identify the possible role of wave-current interactions, we designed an experiment without current effect on waves (using the same wave model equations but omitting the velocity terms as in Weir et al., 2011). In this case, VLF motions are slightly more energetic but not significantly so. Therefore, wave-current interactions play no substantial part in our case and much of our VLF motions results from jet instabilities with properties agreeing with linear instability theories (Eq. 8).

⁶ Due to the current effect on waves, the rip current slows down waves in the rip channel and causes cross-shore pressure gradients and breaking that weakens the rip. This process can be either equilibrated (weakening the rip) or transient for small wave forcing, resulting in rip current oscillations (Kennedy and Zhang, 2008).

⁷ From Cochran's theorem, the standard error of sample variance is $\sqrt{2/(n-1)} \sigma^2$, where n is the number of events and σ^2 the true variance.

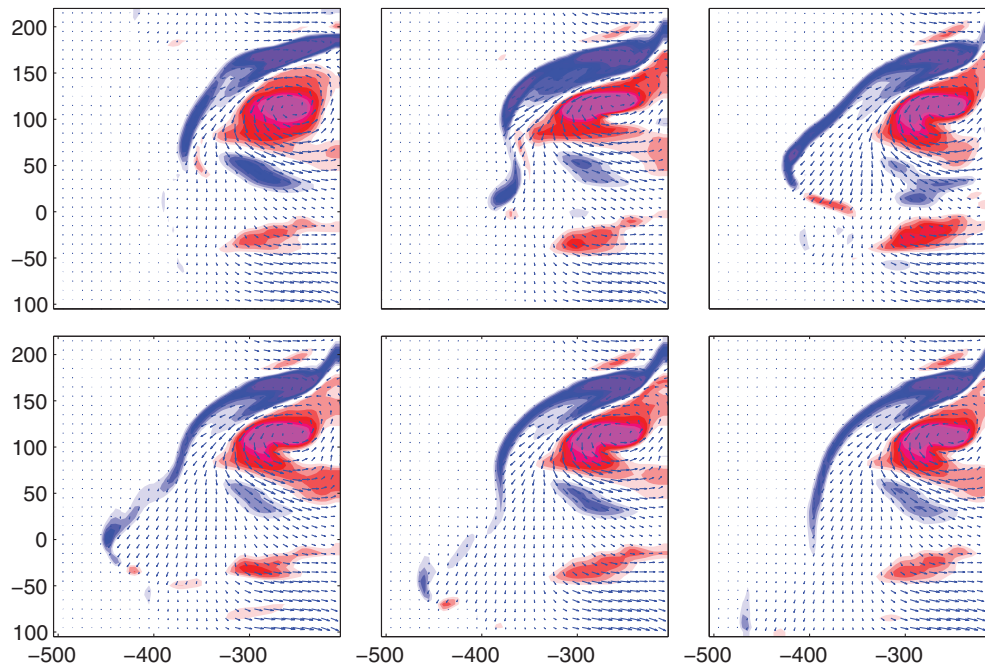


Fig. 11. Sequence of ROMS surface vorticity showing the meandering of rip current from a steady-state simulation (low-energy conditions of June 2007). The sequence reads from left to right and top to bottom. The time interval between frames is 6 min. The color scale of vorticity ranges from $\pm 0.04 \text{ s}^{-1}$.

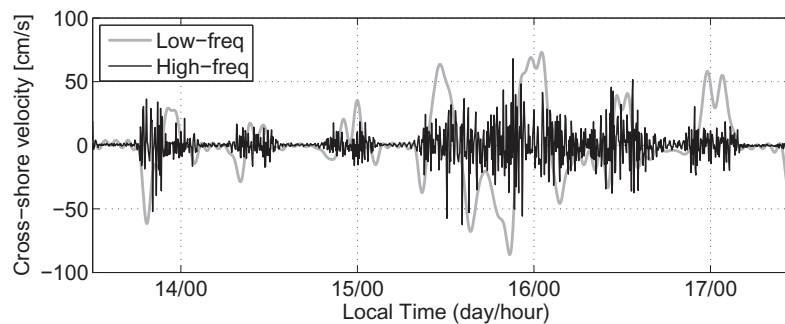


Fig. 12. Low and high-pass filtered cross-shore (wave-averaged) velocity time series from observed data at station S4 (June 13–17 2007). Rip currents are represented by low-pass events (grey curve) and VLF oscillations by the high-pass signal (black curve). The filter's cutoff period is 1 h.

5.5. Resolution convergence and turbulent closure

Part of the missing VLF energy in the model may be related to wave forcing variability not accounted for; another part may be due to still insufficient numerical resolution. Experiments with variable resolution (5, 10, and 20 m) shows that the numerical solution has not reached convergence at 5 m resolution since VLF energy keeps increasing from 20 to 10 and 5 m (especially the higher range of frequencies). Therefore, higher resolution simulations will be needed to assess the maximum energy that can be reached through instability processes.

The question of turbulent closure is of interest for resolution convergence. Here, we use a resolution and flow-dependent Smagorinsky model with coefficient $C_S=0.1$, which is on the order of estimates from Large Eddy Simulations⁸ (Meyers and Sagaut, 2006). Different values of C_S tend to only affect the VLF part of the spectrum (the energy increases/decreases for smaller/larger values). Besides the Smagorinsky coefficient, the choice of closure model can also be questioned with

⁸ In addition to physical closure, numerical closure of the discretized equations is guaranteed by implicit numerical diffusion in ROMS upstream-biased advection scheme (Shchepetkin and McWilliams, 1998). This numerical diffusion is small at resolutions of order 10 m or less.

respect to turbulent regimes. VLF eddies being much larger than local water depth, the turbulent regime would obey a 2D inverse energy cascade and forward enstrophy cascade. Leith model (Leith, 1968) would be more appropriate in this case. An inverse cascade would be consistent with an increase of energy towards lower frequencies in the VLF range.

In any case, bottom friction provides the most important sink for kinetic energy of the rip system. In particular, the VLF energy spectrum is sensitive to bottom roughness (not shown). A decrease of roughness length from 1 cm to 0.1 mm increases VLF energy but at the expense of realistic persistent rip currents (Section 4.2 and Fig. 9). The model parameters appear well constrained in this respect.

5.6. Tridimensional effect

VLF oscillations are nearly absent from 2D simulations. In Fig. 13, all frequencies are considerably weaker than in the 3D model and much weaker than in the data. Consistently, Bruneau et al. (2009a) failed to capture VLF frequencies in their standard 2D simulations and significant viscosity reduction was required to generate instabilities in their case. We interpret this result as evidence that the barotropic component of 2D equations may not produce enough current shear to trigger instability.

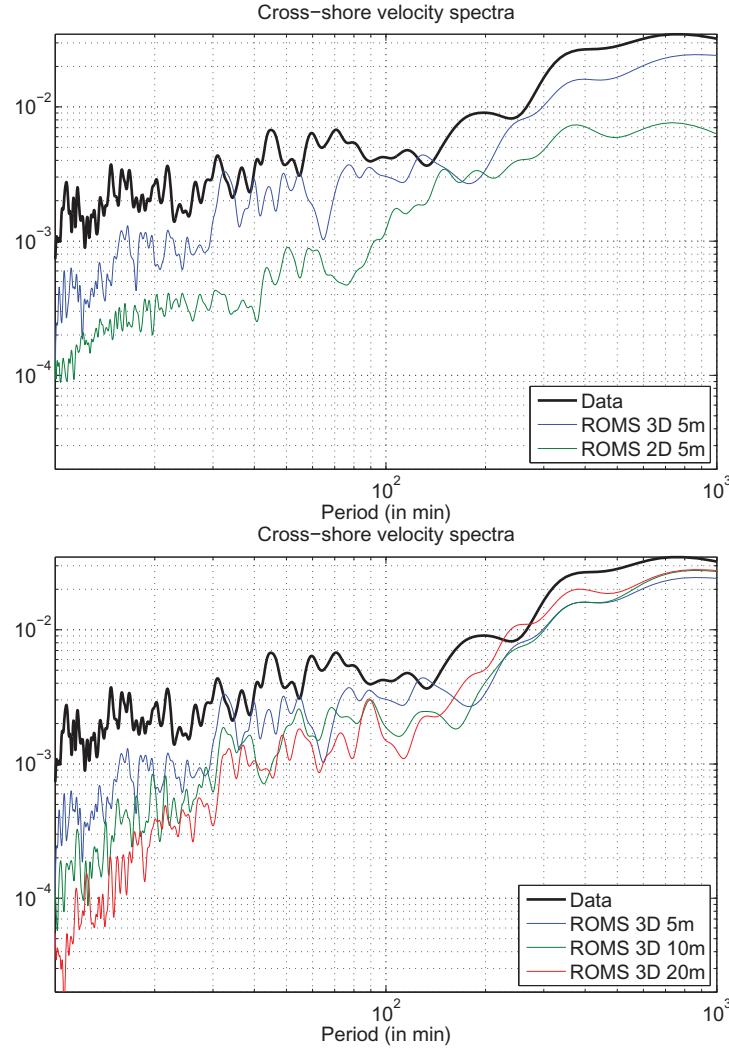


Fig. 13. Frequency spectra of rip neck currents (cross-shore velocity at station S4). The model is compared with *in situ* data from the 5-day Biscarrosse campaign of 2007. The top panel features the 3D and 2D model solutions at 5 m resolution; the bottom panel shows the 3D model at 5, 10, and 20 m resolutions.

In linear models, lateral or bottom friction increases the jet spreading of the classical planar jet solution and causes the centerline velocity to decay more rapidly. We mentioned that the bottom slope acts in the same direction because depth-averaged flow continuity overwhelms the effect of vortex stretching (Haller and Dalrymple, 2001). Interestingly and as already predicted by Arthur (1962), this balance may be affected by tridimensionality. After rip currents leave the surf zone they tend to be confined to a layer of thickness equal to the depth at the seaward edge of the surf zone (Fig. 8). This has a double effect. On one hand, surface confinement reduces bottom interaction and associated stretching effect. On the other hand, bottom friction decreases in the process. More importantly, a surface-intensified jet has more intense centerline velocity than its depth-averaged flow on a sloping beach (due to continuity). From our results, nonlinear interactions between baroclinic and barotropic components also appear to increase the barotropic flow. Overall, the increase of shear production from surface intensification appears to easily dominate over depth-averaged dynamics.

5.7. Analysis of steady-state simulation

To analyze further the intrinsic part of model variability, we designed a statistically stationary experiment (or steady-state simulation) using the low-energy conditions of June 2007 as persistent forc-

ing. This is a rather strong rip event that has the advantage of being relatively isolated from the surrounding circulation, contrarily to the chaotic fields produced by high-energy conditions. The result shows a range of VLF oscillations at about 30 min period in agreement with shear instability scaling (Section 5.1).

To localize in space the instability process, we compute the mean-eddy conversion terms in the stationary experiment (e.g., Marchesiello et al., 2003):

$$KmKe = -\overline{u'u'} \frac{\partial \bar{u}}{\partial x} - \overline{u'v'} \frac{\partial \bar{u}}{\partial y} - \overline{u'v'} \frac{\partial \bar{v}}{\partial x} - \overline{v'v'} \frac{\partial \bar{v}}{\partial y} \quad (9)$$

Here, \bar{u} and u' indicate time-averaged and perturbation fields over the 8 h-long simulation (assuming well-behaved eddy-mean decomposition).

Fig. 15 (left panel) shows $KmKe$ together with contours of strain rate⁹ and velocity vectors. When conversion is positive, it indicates the work of shear instability. In contrast, negative values indicate feedback to the mean flow. The maximum energy conversion to eddies is clearly in the feeder zone, coincidental with a maximum strain rate (essentially a contraction process here). The instability decreases

⁹ The strain rate $|S| = \sqrt{\left[\frac{\partial u}{\partial x} - \frac{\partial v}{\partial y}\right]^2 + \left[\frac{\partial u}{\partial y} + \frac{\partial v}{\partial x}\right]^2}$ is the sum of stretching and shearing strain respectively.

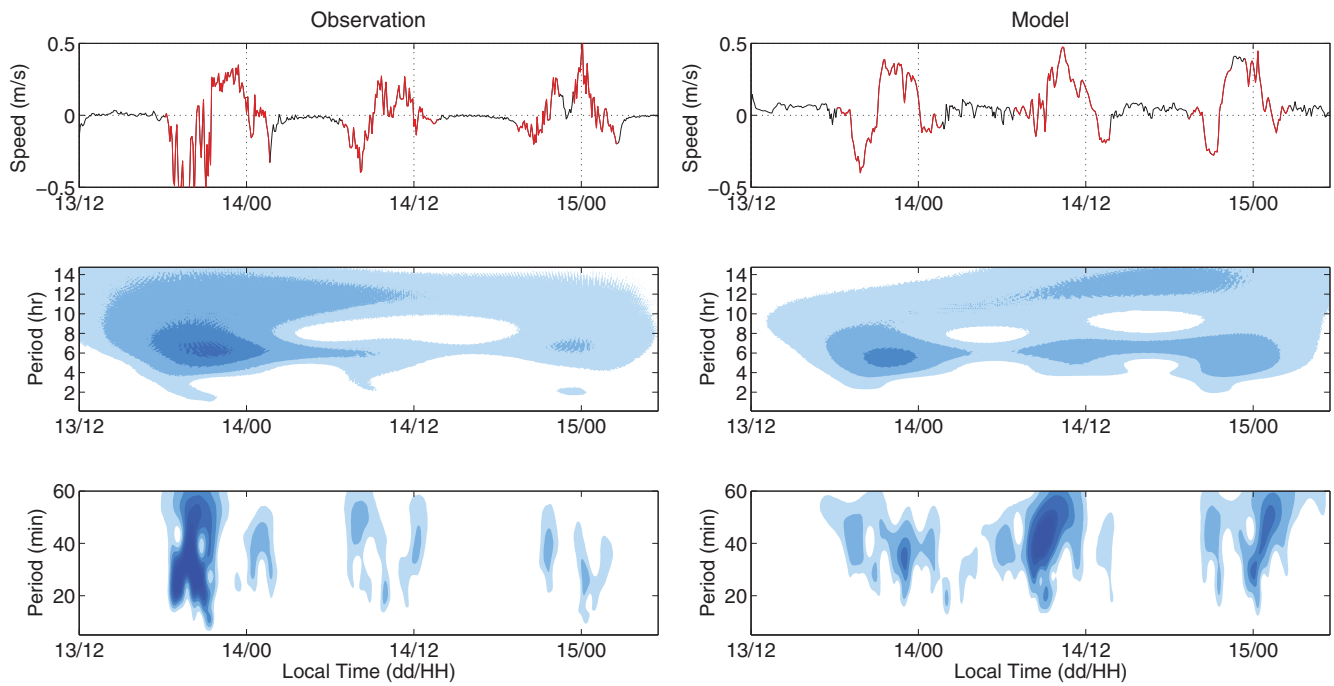


Fig. 14. Morlet wavelet analysis of rip neck (cross-shore velocity at station S4). The model is compared with *in situ* data from the first 2 days of the 2007 Biscarosse campaign, showing 3 rip events. The time series are presented on top with red color during breaking conditions in the rip channel ($\gamma_b > 0.3$). The contours (bottom panels) represent a percentage of the total signal's energy in the time and frequency domain: model and observations are only compared qualitatively here (darker shades indicating higher values). The middle panel shows the entire energy spectrum while the lower panel focuses on the VLF range (in this case, the time-series are first high-pass filtered – 1h – to better extract the VLF peaks; see text). (For interpretation of the references to color in this figure legend, the reader is referred to the web version of this article).

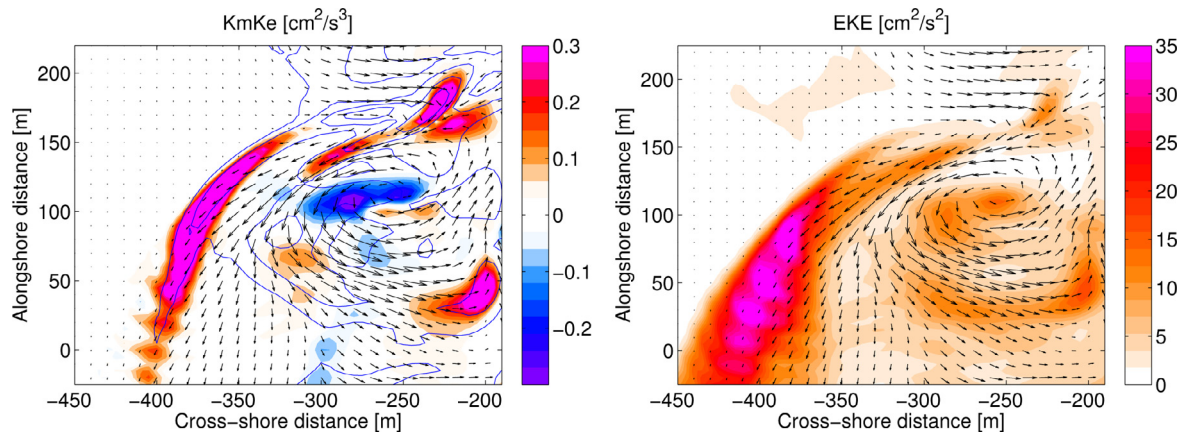


Fig. 15. Mean-eddy conversion KmKe (left) and eddy kinetic energy EKE (right) in the rip current system from an 8 h steady-state simulation of June 2007 low-energy conditions. Strain contours are overlaid in the KmKe figure; velocity vectors in both.

offshore along the jet axis as predicted for sinuous instability modes. However, a new strong maximum appears at the rip head. This area is characterized by surface-trapped currents in relatively deep water, where bottom friction is weaker than in the rip channel. The offshore growth rate of disturbances is thus less impaired by friction. It allows the offshore currents to wander about as a wavy (ribbonlike) sinuous mode (Fig. 11). On the other hand, KmKe is negative in the center and onshore flow area of the cyclonic recirculation cell, suggesting that the onshore flow and recirculation cell are reinforced by advective processes. Consistently, a simulation with increased viscosity (not shown) where no instability can develop produces a weaker recirculation cell. This result is similar to that of Haas et al. (2003) from bottom friction sensitivity experiments.

Fig. 15 (right panel) presents the Eddy kinetic energy (EKE) of this equilibrated solution. The structure of EKE contrasts with that of Eddy production (KmKe; left panel). Both EKE and KmKe have maxima in

the feeder zone but the largest patch of Eddy variability is located offshore at the rip head. Our understanding is that instabilities are mostly generated in the feeder zone but their linear and nonlinear growth are along the jet axis (justifying spatial stability analysis as in Haller and Dalrymple, 2001). The rip channel appears as a stabilizing region, probably due to bottom friction and topographic channeling, but reduced friction in deeper water allows instabilities to grow more freely and produce wavy filaments akin to sinuous modes (Fig. 11).

6. Conclusion

We present some validation of tridimensional rip current modeling in the Aquitanian coastal zone using *in-situ* and remote video sensing. We show the benefits of 3D versus 2D modeling for the simulation of mean rip currents and their low-frequency variability. The 3D model appears also more robust than its 2D counterpart with

respect to parameter sensitivity (bottom friction) as more physics is added to the problem. This idea is reminiscent of that of Weir et al. (2011) regarding the feedback of currents to wave forcing. They found that bottom friction in uncoupled circulation models can be tuned to mimic the behavior of wave-current coupled models, but the latter requires less ad hoc tuning. Here, we conclude that tridimensional nearshore models may provide a valuable and cost-effective alternative to more usual 2D approaches, which miss the vertical flow structure and its nonlinear interaction with the 2D flow.

Our study suggests that intrinsic dynamics of nearshore circulation could explain a large part of low-frequency variability and be a serious alternative to low-frequency wave-forcing in rip currents (or at least a complementary process). There are large implications for the ejection of surf-zone material, i.e. shelf-surf tracer exchanges (Hally-Rosendahl et al., 2014). Recirculation cells would promote retention while pulsation and filament formation would do the opposite and increase dispersion out of the surf-zone. Further study of the intrinsic dynamics of wave-induced nearshore currents is thus of great interest. Questions arise as to the form the surface-intensified offshore jets take in relation to the density stratification and Coriolis force and what is their interaction with other shelf currents. Other questions require a better assessment of instability modes and their nonlinear development; the turbulent regime of nearshore currents; the resolution needed to capture the essential dynamics; and the parametrization of their energy dissipation.

Acknowledgments

This research has received support from grants by ANR (COMODO: ANR-11-MONU-005) and LEFE/INSU (COMODO-WAVES) in France; NSF (OCE-1344970) and ONR (N000141410626) in the USA. It was also granted access to the HPC resources of GENCI-IDRIS under allocation 2014-017298. We thank the EPOC/METHYS coastal dynamics group for providing in-situ data from the June 2007 campaign and Philippe Bonneton for useful discussions. We also thank three anonymous reviewers for their careful reading of our manuscript and their insightful comments and suggestions.

References

- Almar, R., Castelle, B., Ruessink, B.G., Sénéchal, N., Bonneton, P., Mariou, V., 2010. Two- and three-dimensional double-sandbar system behaviour under intense wave forcing and a meso-macro tidal range. *Cont. Shelf Res.* 30 (7), 781–792. <http://dx.doi.org/10.1016/j.csr.2010.02.001>.
- Almar, R., Castelle, B., Ruessink, G., Senechal, N., Bonneton, P., Mariou, V., 2009. High-frequency video observation of a double sandbar system under high-energy wave forcing. *J. Coast. Res.* 56, 1706–1710.
- Antuono, M., Brocchini, M., Bellotti, G., 2007. Integral properties of the swash zone and averaging. part 3. longshore shoreline boundary conditions for wave-averaged nearshore circulation models. *J. Fluid Mech.* 573, 399–415.
- Arthur, R., 1962. A note on the dynamics of rip currents. *J. Geophys. Res.* 67 (7), 2778–2779.
- Bickley, W., 1939. The plane jet. *Philos. Mag. Ser. 7*, 727–731.
- Blaas, M., Dong, C., Marchesiello, P., McWilliams, J.C., Stolzenbach, K.D., 2007. Sediment-transport modeling on southern californian shelves: a ROMS case study. *Cont. Shelf Res.* 27 (6), 832–853. <http://dx.doi.org/10.1016/j.csr.2006.12.003>.
- Brocchini, M., Bellotti, G., 2002. Integral flow properties of the swash zone and averaging. part 2. shoreline boundary conditions for wave-averaged models. *J. Fluid Mech.* 458, 269–281.
- Bruneau, N., Bonneton, P., Castelle, B., Pedreros, R., 2011. Modeling rip current circulations and vorticity in a high-energy mesotidal-macrotidal environment. *J. Geophys. Res.: Oceans* 116 (C7). doi:10.1029/2010JC006693.
- Bruneau, N., Castelle, B., Bonneton, P., Pedreros, R., 2009a. Very low frequency motions of a rip current system: observations and modeling. *J. Coast. Res.* 56 (2), 1731–1735.
- Bruneau, N., Castelle, B., Bonneton, P., Pedreros, R., Almar, R., Bonneton, N., Bretel, P., Parisot, J.-P., Sénéchal, N., 2009b. Field observations of an evolving rip current on a meso-macrotidal well-developed inner bar and rip morphology. *Cont. Shelf Res.* 29 (14), 1650–1662.
- Butel, R., Dupuis, H., Bonneton, P., 2002. Spatial variability of wave conditions at french atlantic coast using in-situ data. *J. Coast. Res.* 36, 96–108.
- Castelle, B., Bonneton, P., Dupuis, H., Senechal, N., 2007. Double bar beach dynamics on the high-energy meso-macrotidal french aquitanian coast : a review. *Mar. Geol.* 245 (141–159).
- Church, J.C., Thornton, E.B., 1993. Effects of breaking wave induced turbulence within a longshore current model. *Coast. Eng.* 20 (1–2), 1–28. [http://dx.doi.org/10.1016/0378-3839\(93\)90053-B](http://dx.doi.org/10.1016/0378-3839(93)90053-B).
- De Vriend, H.J., Stive, M.J.F., 1987. Quasi-3d modelling of nearshore currents. *Coast. Eng.* 11 (5–6), 565–601. [http://dx.doi.org/10.1016/0378-3839\(87\)90027-5](http://dx.doi.org/10.1016/0378-3839(87)90027-5).
- Debreu, L., Marchesiello, P., Penven, P., Cambon, G., 2012. Two-way nesting in split-explicit ocean models: algorithms, implementation and validation. *Ocean Modell.* 49–50 (0), 1–21. <http://dx.doi.org/10.1016/j.ocemod.2012.03.003>.
- Haas, K.A., Svendsen, I.A., 2002. Laboratory measurements of the vertical structure of rip currents. *J. Geophys. Res.: Oceans* 107 (C5), 15–1–15–19. doi:10.1029/2001JC000911.
- Haas, K.A., Svendsen, I.A., Haller, M.C., Zhao, Q., 2003. Quasi-three-dimensional modeling of rip current systems. *J. Geophys. Res.: Oceans* 108 (C7), 3217. doi:10.1029/2002JC001355.
- Haller, M.C., Catalán, P.A., 2009. Remote sensing of wave roller lengths in the laboratory. *J. Geophys. Res.: Oceans* 114 (C7). doi:10.1029/2008JC005185.
- Haller, M.C., Dalrymple, R.A., 2001. Rip current instabilities. *J. Fluid Mech.* 433, 161–192. doi:10.1017/S0022112000003414.
- Hally-Rosendahl, K., Feddersen, F., Guza, R.T., 2014. Cross-shore tracer exchange between the surfzone and inner-shelf. *J. Geophys. Res.: Oceans* 119 (7), 4367–4388. doi:10.1002/2013JC009722.
- Holland, K.T., Holman, R.A., Lippmann, T.C., Stanley, J., Plant, N., 1997. Practical use of video imagery in nearshore oceanographic field studies. *IEEE J. Oceanic Eng.* 22 (1), 81–92.
- Holman, R., Haller, M.C., 2013. Remote sensing of the nearshore. *Annu. Rev. Mar. Sci.* 5 (1), 95–113.
- Kennedy, A.B., 2003. A circulation description of a rip current neck. *J. Fluid Mech.* 497, 225–234. doi:10.1017/S0022112003006827.
- Kennedy, A.B., Zhang, Y., 2008. The stability of wave-driven rip current circulation. *J. Geophys. Res.: Oceans* 113 (C3). doi:10.1029/2006JC003814.
- Leith, C.E., 1968. Diffusion approximation for two dimensional turbulence. *Phys. Fluids* (1958–1988) 11 (3), 671–672.
- Lippmann, T.C., Holman, R.A., 1989. Quantification of sand bar morphology: a video technique based on wave dissipation. *J. Geophys. Res.: Oceans* 94 (C1), 995–1011. doi:10.1029/JC094iC01p00995.
- Long, J.W., Özkan-Haller, H.T., 2009. Low-frequency characteristics of wave group-forced vortices. *J. Geophys. Res.-Oceans* 114 (C08004).
- MacMahan, J.H., Reniers, A.J.H.M., Thornton, E.B., Stanton, T.P., 2004. Surf zone eddies coupled with rip current morphology. *J. Geophys. Res.: Oceans* 109 (C7). doi:10.1029/2003JC002083.
- MacMahan, J.H., Thornton, E.B., Reniers, A.J., 2006. Rip current review. *Coast. Eng.* 53 (2–3), 191–208. <http://dx.doi.org/10.1016/j.coastaleng.2005.10.009>. Coastal Hydrodynamics and Morphodynamics Symposium celebrating the academic closing address of Jurjen A. Battjes.
- Marchesiello, P., McWilliams, J.C., Shchepetkin, A., 2001. Open boundary conditions for long-term integration of regional oceanic models. *Ocean Modell.* 3 (1–2), 1–20. doi:10.1016/S1463-5003(00)00013-5.
- Marchesiello, P., McWilliams, J.C., Shchepetkin, A., 2003. Equilibrium structure and dynamics of the california current system. *J. Phys. Oceanogr.* 33, 753–783.
- McWilliams, J.C., Restrepo, J.M., Lane, E.M., 2004. An asymptotic theory for the interaction of waves and currents in coastal waters. *J. Fluid Mech.* 511, 135–178. doi:10.1017/S0022112004009358.
- Meyers, J., Sagaut, P., 2006. On the model coefficients for the standard and the variational multi-scale smagorinsky model. *J. Fluid Mech.* 569, 287–319.
- Özkan-Haller, H.T., Li, Y., 2003. Effects of wave-current interaction on shear instabilities of longshore currents. *J. Geophys. Res.: Oceans* 108 (C5). doi:10.1029/2001JC001287.
- Penven, P., Debreu, L., Marchesiello, P., McWilliams, J., 2006. Evaluation and application of the roms 1-way embedding procedure to the central california upwelling system. *Ocean Modell.* 12 (1–2), 157–187. doi:10.1016/j.ocemod.2005.05.002.
- Peregrine, D.H., 1998. Surf zone currents. *Theor. Comput. Fluid Dyn.* 10, 295–309.
- Shchepetkin, A.F., McWilliams, J.C., 1998. Quasi-monotone advection schemes based on explicit locally adaptive dissipation. *Mon. Weather Rev.* 126, 1541–1580.
- Shchepetkin, A.F., McWilliams, J.C., 2005. The regional oceanic modeling system (roms): a split-explicit, free-surface, topography-following-coordinate oceanic model. *Ocean Modell.* 9 (4), 347–404. <http://dx.doi.org/10.1016/j.ocemod.2004.08.002>.
- Shepard, F.P., Emery, K.O., Fond, E.C.L., 1941. Rip currents: a process of geological importance. *J. Geol.* 49 (4), 337–369.
- Smagorinsky, J., 1963. General circulation experiments with the primitive equations. *Mon. Weather Rev.* 91 (3), 99–164. doi:10.1175/1520-0493(1963)091<0099:GCEWTP>2.3.CO;2.
- Soulsby, R., 1995. Bed shear stresses due to combined waves and currents. In: Stive, M., Fredsøe, J., Hamm, L., Soulsby, R., Teisson, C., Winterwerp, J. (Eds.), *Advances in Coastal Morphodynamics*. Delft Hydraulics, Delft, The Netherlands, pp. 420–423.
- Spydell, M., Feddersen, F., 2009. Lagrangian drifter dispersion in the surf zone: directionally spread, normally incident waves. *J. Phys. Oceanogr.* 39 (4), 809–830. doi:10.1175/2008JPO3892.1.
- Uchiyama, Y., McWilliams, J., Shchepetkin, A., 2010. Wave-current interaction in an oceanic circulation model with a vortex-force formalism: application to the surf zone. *Ocean Modell.* 34, 16–35.
- Uchiyama, Y., McWilliams, J.C., Restrepo, J.M., 2009. Wave-current interaction in nearshore shear instability analyzed with a vortex force formalism. *J. Geophys. Res.: Oceans* 114 (C6). doi:10.1029/2008JC005135.

- Warner, J.C., Defne, Z., Haas, K., Arango, H.G., 2013. A wetting and drying scheme for ROMS. *Comput. Geosci.* 58, 54–61. <http://dx.doi.org/10.1016/j.cageo.2013.05.004>.
- Weir, B., Uchiyama, Y., Lane, E.M., Restrepo, J.M., McWilliams, J.C., 2011. A vortex force analysis of the interaction of rip currents and surface gravity waves. *J. Geophys. Res.: Oceans* 116 (C5). doi:[10.1029/2010JC006232](https://doi.org/10.1029/2010JC006232).
- Wright, L., Short, A., 1984. Morphodynamic variability of surf zones and beaches: a synthesis. *Mar. Geol.* 56, 93–118.
- Yu, J., Slinn, D.N., 2003. Effects of wave-current interaction on rip currents. *J. Geophys. Res.: Oceans* 108 (C3). doi:[10.1029/2001JC001105](https://doi.org/10.1029/2001JC001105).